ADVANCED MATERIALS

Supporting Information

for *Adv. Mater.*, DOI: 10.1002/adma.201401917

Novel Electroforming-Free Nanoscaffold Memristor with Very High Uniformity, Tunability, and Density

*Shinbuhm Lee, Abhijeet Sangle, Ping Lu, Aiping Chen, Wenrui Zhang, Jae Sung Lee, Haiyan Wang, Quanxi Jia, and Judith L. MacManus-Driscoll**

Supporting Information

Novel electroforming-free nanoscaffold memristor with very high uniformity, tunability, and density

*Shinbuhm Lee, Abhijeet Sangle, Ping Lu, Aiping Chen, Wenrui Zhang, Jae Sung Lee, Haiyan Wang, Quanxi Jia, and Judith L. MacManus-Driscoll**

Dr. S. Lee, A. Sangle, Prof. J. L. MacManus-Driscoll
Department of Materials Science and Metallurgy, University of Cambridge
27 Charles Babbage Road, Cambridge, CB3 0FS, United Kingdom
E-mail: jld35@cam.ac.uk

Dr. P. Lu
Sandia National Laboratories
Albuquerque, New Mexico 87185, United States

W. Zhang, Prof. H. Wang
Department of Electrical and Computer Engineering, Texas A&M University
College Station, Texas 77843, United States

Dr. J. S. Lee
School of Physics, Korea Institute for Advanced Study
Seoul 130-722, Republic of Korea

Dr. A. Chen, Dr. Q. X. Jia
Center for Integrated Nanotechnologies, Los Alamos National Laboratory
Los Alamos, New Mexico 87545, United States

Keywords: memristor, nanoscaffold film

Experimental Section

We measured the resistances using a simple two-probe station and a Keithley 2440 source-meter. We used 17-nm-thick samples, grown at the laser repetition rate of 1 Hz, for most of the measurements. However, thicker films of up to 125 nm also showed very similar electroresistance effects, *i.e.* there were no tight constraints on the film thickness requirement. For all the electrical measurements, the Nb-doped $SrTiO_3$ substrate is grounded and the voltage is applied to the Pt electrodes. The pulses of 16 ms duration were applied due to limitation of pulse duration of computer-controlled Keithley 2440 source-meter. To measure electrical characteristics with temperature variation from 20 to 550 ^{o}C, we used a probe station equipped with a hot plate.

To investigate local conduction at vertical interfaces, we employed Agilent 5500 scanning probe microscope. Commercial silicon tips coated with chromium/platinum were used for conductive AFM.

X-ray diffraction was carried out with a Panalytical Empyrean high resolution x-ray diffractometer using Cu-$K\alpha$ radiation (λ = 1.5405 Å). We employed x-ray reflectivity to measure the film thickness.

A FEI Titan^{TM} G2 80-200 STEM with a Cs probe corrector and ChemiSTEM^{TM} technology (X-FEG^{TM} and SuperX^{TM} EDS with four windowless silicon drift detectors), operated at 200 kV was used to evaluate both the structural and chemical properties across the interface. The instrument is also equipped with Gatan EELS system (Quantum SE/963) for EELS analysis. Chemical mapping (EDS or EELS) was acquired along the $SrTiO_3$ [100] zone axis with an electron probe of size less than 0.18 nm, convergence angle of 18.4 mrad and current of ~100 pA. HAADF images were recorded under similar optical conditions with an annular detector having collection range of 60–160 mrad. For EDS atomic-scale chemical mapping, EDS spectral imaging data were acquired as a series of frames, where the same region was scanned multiple time and spatially drift-corrected to build up the spectral imaging

data. The instantaneous dwell time on each pixel was 100 μs. A typical frame was 512 × 128 pixels (pixel size of ~0.02 nm × 0.02 nm). The longer dimension is perpendicular to the interface. The EDS spectral image collection typically took about 1800 s, yielding a total per-pixel dwell time of about 25 ms. EELS spectral imaging data was collected as a line-profile of 128 pixels (pixel size of ~0.08 nm) with per-pixel dwell time of about 200 ms and at a detector semi-angle of ~15 mrad. Sixteen EELS line-profiles across the interface from a similar location were acquired and averaged to minimize the possible artifacts due to elastic scattering of the electron probe within each phase at the atomic-scale.

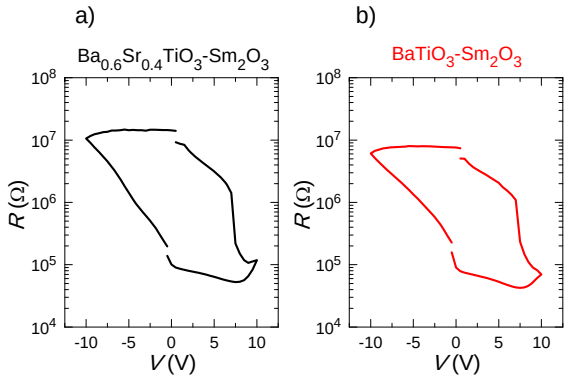

Figure S1. Memristive resistance–voltage (*R*–*V*) curves in nanoscaffold films. a) $Ba_{0.6}Sr_{0.4}TiO_3$-Sm_2O_3 nanoscaffold films. b) $BaTiO_3$-Sm_2O_3 nanoscaffold films. Irrespective of composites of different materials, all nanoscaffold films show similar *R*–*V* curves to nanoscaffold $SrTiO_3$-Sm_2O_3 films in Figure 2a.

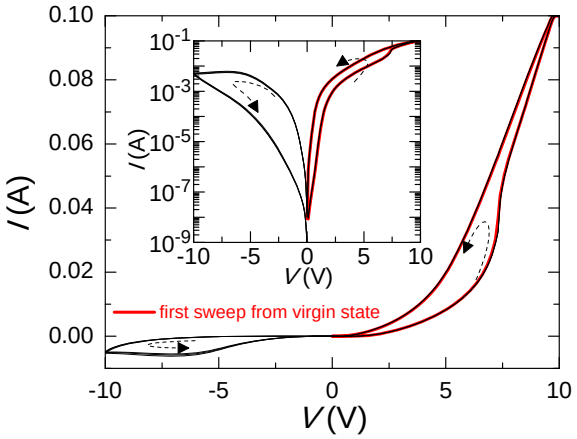

Figure S2. Pinched current–voltage (*I*–*V*) hysteresis loops in nanoscaffold $SrTiO_3$-Sm_2O_3 films. As shwon by the red line, *I*–*V* curve measured by the first sweep from a virgin state is almost same to the successive *I*–*V* curves, meaning that the electroresistance occurs without the electroforming process. This is much clearer in a logarithmic *y*-scale graph, as shown in the inset.

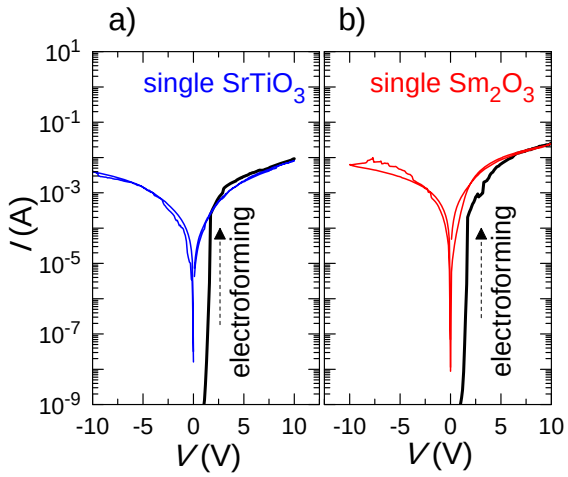

Figure S3. *I–V* curves in single-phase oxide films. a) and b) Electroforming in single $SrTiO_3$ film and in single Sm_2O_3 film. Both $SrTiO_3$ and Sm_2O_3 films are highly insulating in virgin states. When we apply a high voltage in their virgin states, current flow increases abruptly (black lines). After this irreversible electroforming, conductance of $SrTiO_3$ (blue lines) and Sm_2O_3 (red lines) films becomes much higher than their virgin states.

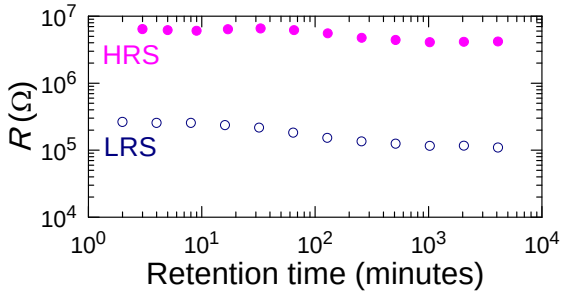

Figure S4. Long retention time. To read the resistance, we applied +0.1 V in a logarithmic time scale. Both HRS and LRS are well preserved up to 4100 minutes (≈ 3 days) without any significant changes.

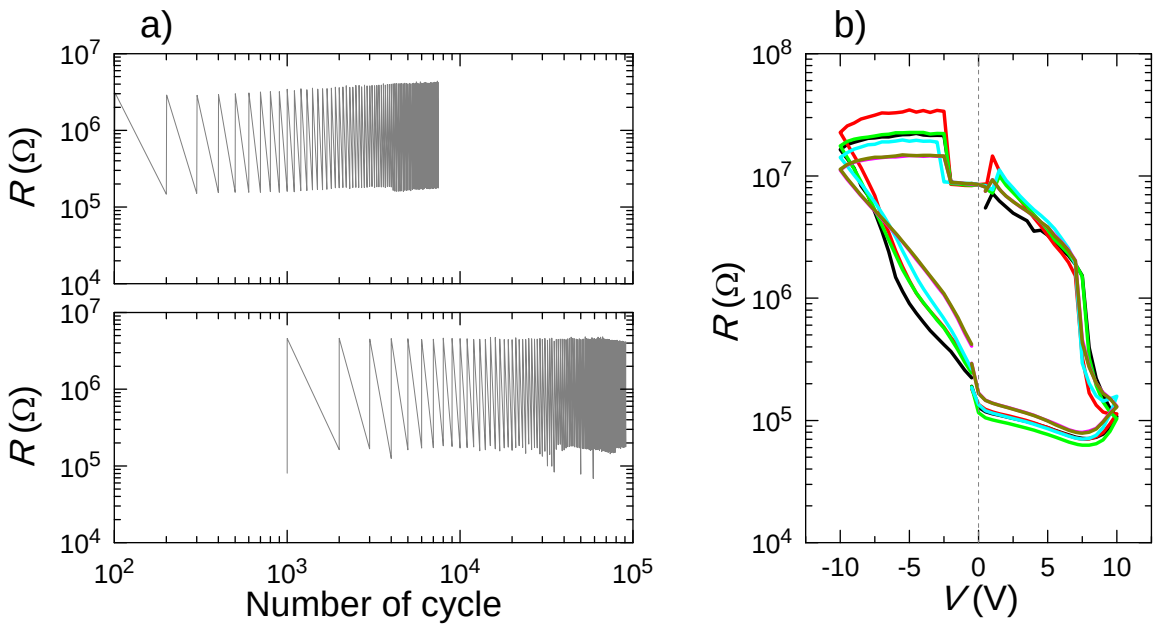

Figure S5. Reproducibility of uniform endurance and memristive *R*–*V* curves. a) and b) We randomly selected the devices to investigate the uniform endurance and the memristive *R*–*V* curves. Both are reproducible from device to device.

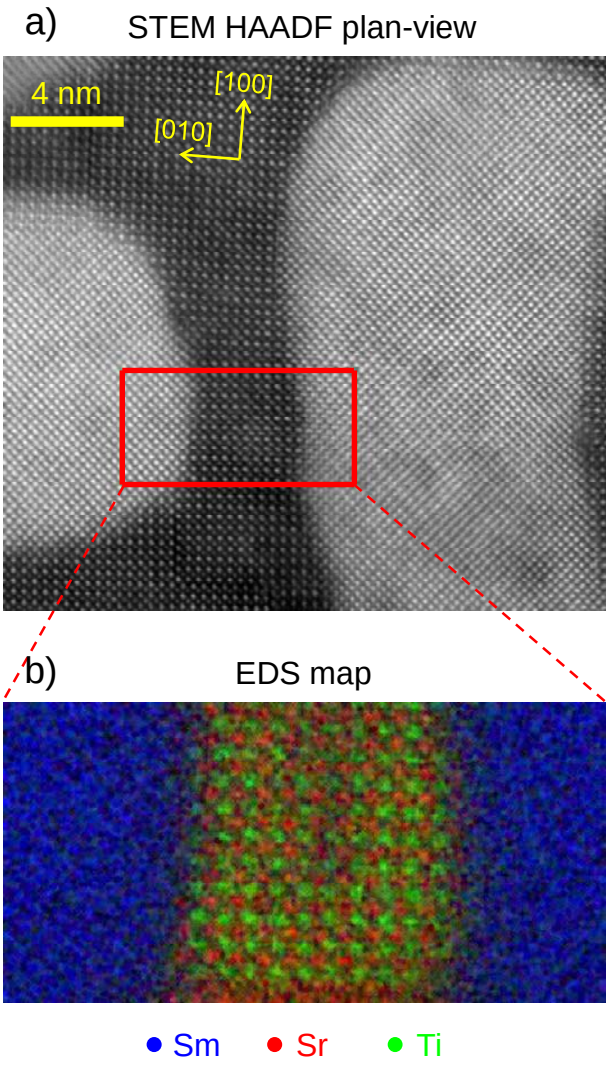

Figure S6. Spectroscopic imaging of atomic elements in nanoscaffold $SrTiO_3$-Sm_2O_3 film using energy-dispersed x-ray spectroscopy (EDS). a) Scanning transmission electron microscopy (STEM) high-angle annular dark-field (HAADF) image in plan-view. The matrix and nanocolumns correspond to the dark and bright contrasts. The red rectangular area is tested. b) Atomic element mapping using EDS. The EDS image clearly shows distribution of Sm (blue) in the bright contrast, and Sr (red) and Ti (green) atoms in the dark contrast. The bright and dark contrasts are assigned to Sm_2O_3 nanocolumns and $SrTiO_3$ matrix, respectively.

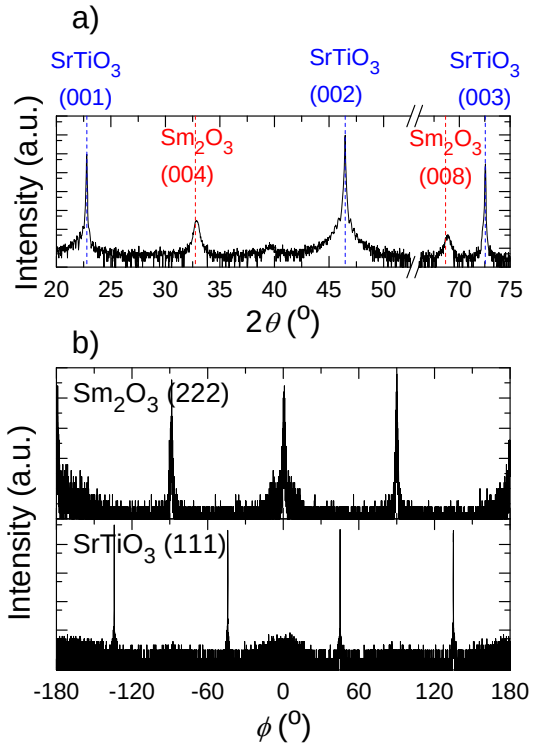

Figure S7. Crystallographic investigation of nanoscaffold $SrTiO_3$-Sm_2O_3 film using x-ray diffraction. a) Out-of-plane epitaxial relationship investigation by ω–2θ scan. All of the observed peaks correspond to (00*l*) peaks of $SrTiO_3$ and Sm_2O_3, indicating preferential orientation of Sm_2O_3 film on Nb-doped $SrTiO_3$ substrate. The (00*l*) peaks of $SrTiO_3$ film cannot be distinguished from those of Nb-doped $SrTiO_3$ substrate. There are no peaks of intermixing phases of $SrTiO_3$ and Sm_2O_3. b) In-plane epitaxial relationship investigation by phi scan. The top and bottom panels show 360° phi scans of the Sm_2O_3 (222) film and $SrTiO_3$ (111) substrate reflections. The film and substrate peaks are separated by 45°, revealing the in-plane relationship of $Sm_2O_3[110] \| SrTiO_3[100]$.

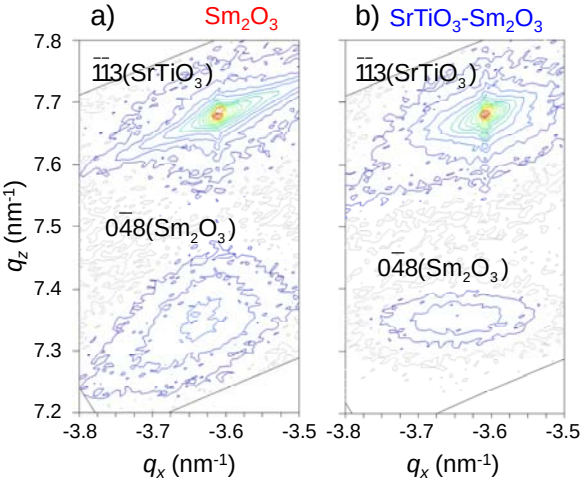

Figure S8. Reciprocal space maps about the $(\bar{1}\bar{1}3)$ $SrTiO_3$ substrate. a) For single Sm_2O_3 films, the broad $(0\bar{4}8)$ Sm_2O_3 peak in q_z-axis indicates a wide spread of lattice parameters. b) For the $SrTiO_3$-Sm_2O_3 nanoscaffold films, the $(0\bar{4}8)$ Sm_2O_3 peak in q_z-axis is much sharper and narrower, indicating little spread of the lattice parameters. We cannot find any peaks of the $SrTiO_3$ matrix near the SrTiO3 substrate peak. This indicates that the cell volume of the $SrTiO_3$ matrix is very close to that of substrate. Hence, in the nanoscaffold film, both Sm_2O_3 and $SrTiO_3$ are well crystallized and their lattice constants are uniform through the thickness of the film. The very high quality of the nanoscaffold films was also observed in nanoscaffold $BaTiO_3$-Sm_2O_3 [Ref. S1] and $Ba_{0.6}Sr_{0.4}TiO_3$-Sm_2O_3 [Ref. S2] films.

Numerical calculation of τ by considering the Joule-heating-accelerated drift of oxygen vacancies

It was theoretically derived[S3] that the ionic drift can cause the exponentially varying behavior of the transient time τ on an external voltage, as shown in Figure 4e in the main text. This is due to the exponential variation of the drift velocity of the ion depending on an external electric field in the following equation.

$$v = fae^{-\frac{U_A}{k_B T}} \sinh\left(\frac{qEa}{2k_B T}\right),$$

where v is the drift velocity of the ion, f is the frequency of escape attempts, U_A is the activation energy for ion hopping, a is the periodicity of the potential energy barrier, k_B is the Boltzmann's constant, T is the local temperature, q is the amount of charge which the ion carries, and E is an applied electric field. In this study, the moving ion is an oxygen ion or oxygen vacancy, thus, $q = 2e$ where e is the elementary charge. Figure S9 shows the schematic diagram of the Sm_2O_3-$SrTiO_3$ device. As explained in the main text, oxygen vacancies are produced from the lattice mismatch and move along the vertical interfaces of Sm_2O_3-$SrTiO_3$. The oxygen vacancies are assumed to move over a certain distance l, resulting in a high to low resistance-switching process during τ. Then, τ is given by (see Equation (11) in Ref. S4)

$$\tau = \frac{l}{v} = \frac{l}{fa} e^{\frac{U_A}{k_B T}} \sinh^{-1}\left(\frac{qV_{\text{int}} a}{2l_{\text{int}} k_B T}\right), \qquad \text{(S1)}$$

where V_{int} is the voltage applied to the interface, l_{int} is the length of the interface (8 or 17 nm), and $E = V_{\text{int}}/l_{\text{int}}$ is used. Equation S1 clearly shows the exponential behavior of τ on voltage.

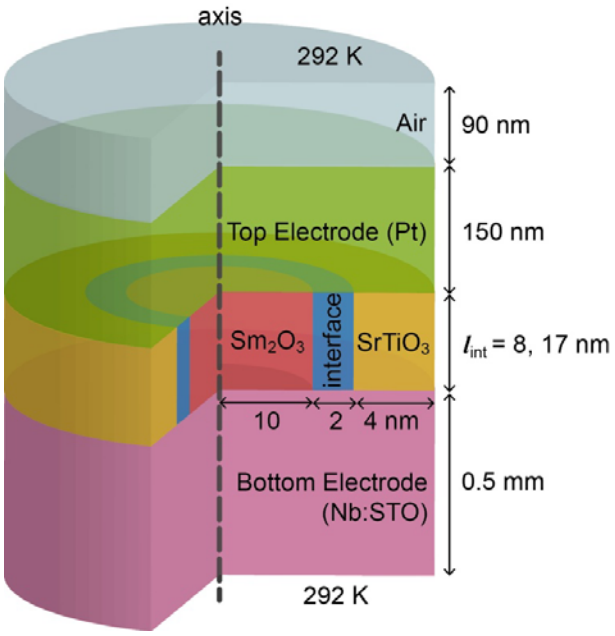

Figure S9. Schematic diagram of the Sm_2O_3-$SrTiO_3$ device. The temperature of the top and bottom is held fixed at ambient temperature 292 K. The temperature for the side wall is not fixed since it is assumed to be the middle points between the two Sm_2O_3 nanocolumns.

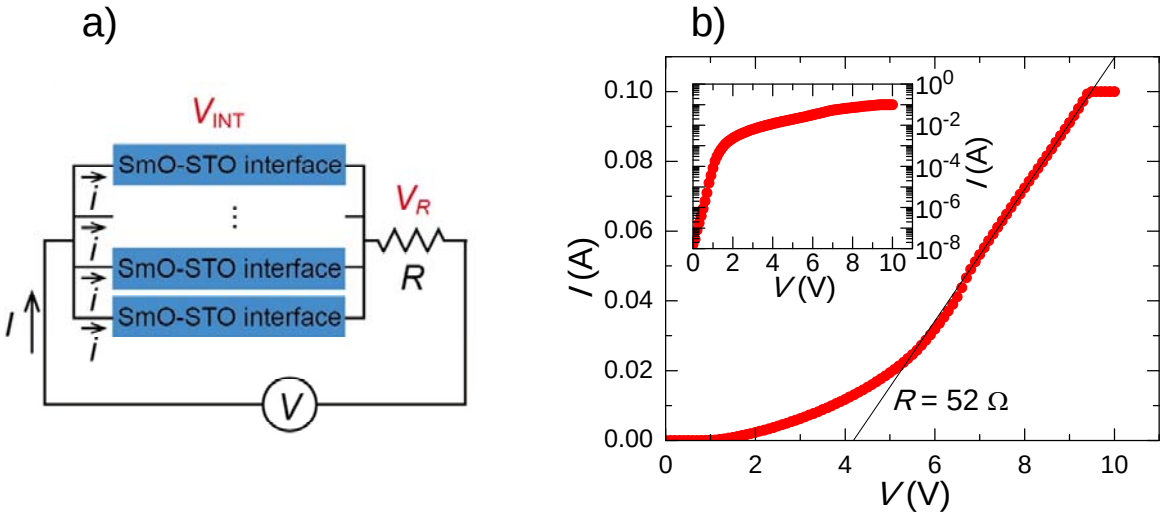

Figure S10. The effect of the remnant resistance. a) Schematic diagram for the circuit of our experiment. b) *I*–*V* curve obtained from high resistance state of the 8-nm-thick device. The inset shows the same *I*–*V* curve with a logarithmic y scale.

The experimentally observed exponential behavior cannot be explained by only the voltage dependence. This is because V_{int} is not the same as the total external voltage V as shown in Figure S10a. In the figure, R is the remnant resistance of the circuit originating from the contact resistance, the bottom and top electrodes and voltage supplier. Then, V_{int} is given by

$$V_{int} = V - IR, \quad \text{(S2)}$$

where I is the total current. Note that $i = I/N_{int}$, where N_{int} (~ 7.7×10^6) is the number of Sm_2O_3 nanocolumns which are inside the area of the circular Pt electrode with 50-μm-radius. Figure S10b shows an I–V curve for l_{int} = 8 nm when the device is in the high-resistance state. The inset shows the same I–V curve with logarithmic scale in y axis. As shown in the figures, the current increases exponentially for the low voltage. For higher voltage, we found that the I–V curve approaches $R \approx 52\ \Omega$ line. This is reasonable because the intrinsic resistance of the voltage supply is 50 Ω.

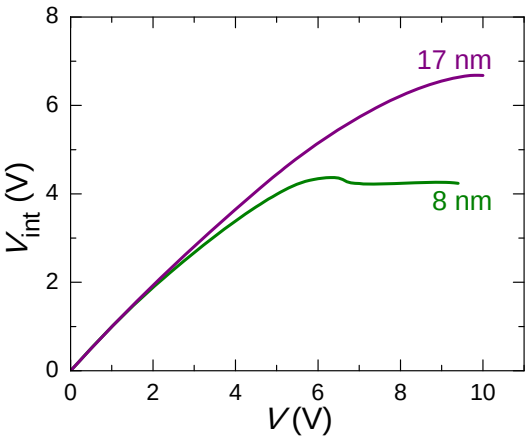

Figure S11. Calculated V_{int} for 8 and 17 nm devices.

Figure S11 shows the calculated V_{int} as a function of V using Equation S2 and the I–V data for l_{int} = 8 and 17 nm devices. As the figure shows, V_{int} seems to saturate at some value for large V, which results in the saturation of τ (see Equation S1) instead of the exponential

decrease. To clearly show this point, we fitted the data of Figure 4e in the main text using Equation S1 with fixed T = 292 K. The best fit was obtained with reasonable fitting parameters: $f = 2.5\times10^{13}$ Hz,[S5] U_A = 0.9 eV,[S4] $a \sim 0.5$ nm.[S4] The results are denoted as dashed lines (purple for 17 nm and green for 8 nm) in Figure S12. The calculated curves are well fitted to the experimental data for small V, but they are no longer decreased, thus, deviating from the data for large V as expected.

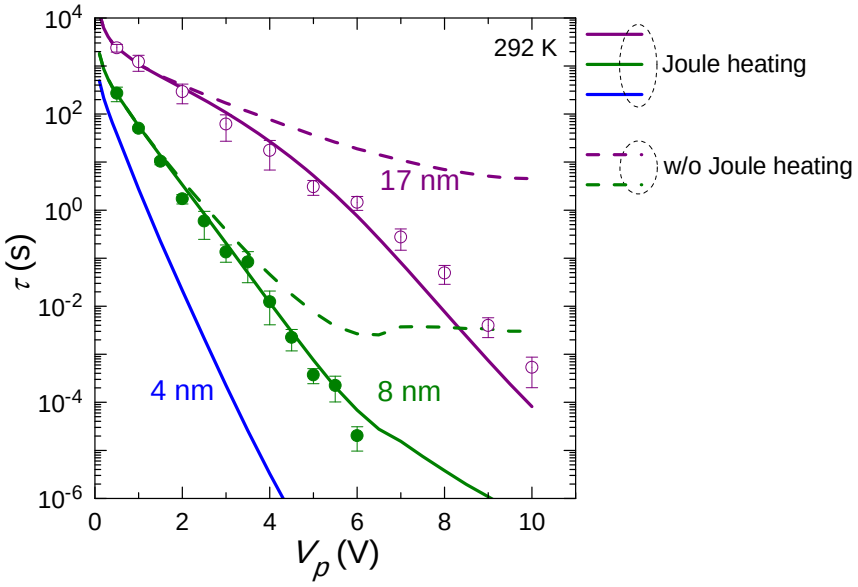

Figure S12. Plot for the transient time τ as a function of V. Purple and green dots are experimental data for 17 and 8 nm devices, respectively. Purple and green dashed lines are theoretical lines without Joule heating effect for 17 and 8 nm devices, respectively. Purple and green solid lines are theoretical lines with Joule heating effect for 17 and 8 nm devices, respectively. Blue solid line is the estimated τ for 4 nm device.

This discrepancy implies that the Joule heating is another important factor to determine τ in this system. As seen in Equation S1, τ can exponentially decrease when T increases. To quantitatively analyse the Joule heating effect, we performed the finite element method simulation on the structure shown in Figure S9 to solve the heat equation

$$c_p \rho \frac{dT}{dt} = -\nabla (k \nabla T) + Q ,$$

where c_p is the specific heat, ρ is the mass density, k is the thermal conductivity, Q is the Joule heat power density. The material parameters are listed in the Table S1. Figure S13a and b show the temperature of the interface (T) as a function of the simulation time (t) for 8 and 17 nm devices, respectively. Note that the difference of the maximum and minimum temperature in the interface is smaller than 0.1 K. We can see that the temperature saturates within 10^{-5} s. The insets show the saturated temperature of the interface as a function of V. We note that the temperature increase for $V < 1.0$ V is negligible. Therefore, when 0.5 V is applied to the device, the local temperature of the interface is the same as the ambient temperature. Thus, the Arrhenius fitting in Figure 4d of the main text is meaningful.

Table S1. Material parameters, used in the numerical simulation

	Pt	$SrTiO_3$	Nb:$SrTiO_3$	Sm_2O_3	Interface	air
k (W/cm K)	0.72 [S6]	0.122 [S4]	0.12 [S4]	0.012 [S7]	0.1 [S9]	0.000243 [S10]
ρ (g/cm^3)	22 [S6]	5.13 [S4]	5.13 [S4]	8.347 [S8]	6.7 [S9]	0.00129 [S10]
c_p (J/g K)	0.13 [S6]	0.538 [S4]	0.538 [S4]	0.745 [S7]	0.6 [S9]	1.0005 [S10]

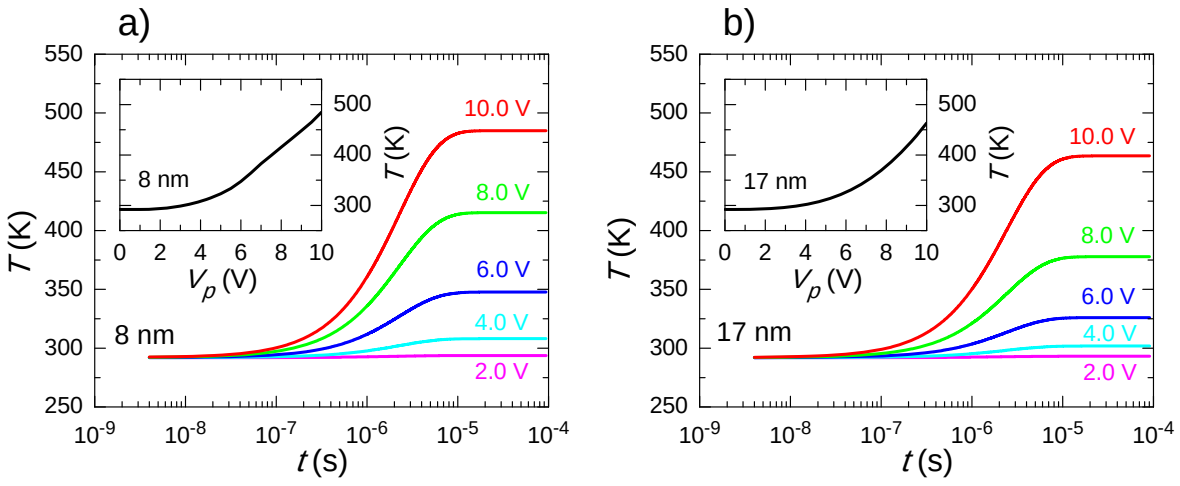

Figure S13. Temperature increase of the interface region. a) 8 nm. b) 17 nm.

With these Joule heating effect, we recalculated Equation S1. The results are denoted by solid lines (purple for 17 nm and green for 8 nm) in Figure S12. The figure clearly shows that the Joule heating effect is an important factor for the exponential decrease of τ. We also estimated τ for a l_{int} = 4 nm device (blue line in Figure S12) based on the *I–V* curve of the 8 nm device. This shows that 10 ns switching is possible within 6 V.

References

[S1] S. A. Harrington, J. Zhai, S. Denev, V. Gopalan, H. Wang, Z. Bi, S. A. T. Redfern, S.-H. Baek, C. W. Bark, C.-B. Eom, Q. X. Jia, M. E. Vickers. J. L. MacManus-Driscoll, *Nature Nanotech.* **2011**, *6*, 491.

[S2] O. J. Lee, S. A. Harrington, A. Kursumovic, E. Defay, H. Wang, Z. Bi, C.-F. Tsai, L. Yan, Q. X. Jia, J. L. MacManus-Driscoll, *Nano Lett.* **2012**, *12*, 4311.

[S3] D. B. Strukov, R. S. Williams, *Appl. Phys. A* **2009**, *94*, 515.

[S4] S. Menzel, M. Waters, A. Marchewka, U. Böttger, R. Dittmann, R. Waser, *Adv. Func. Mater.* **2011**, *21*, 4487.

[S5] S. H. Jeon, W.-J. Son, B. H. Park, S. Han,. *Appl. Phys. A* **2011**, *102*, 909.

[S6] S. H. Chang, S. C. Chae, S. Lee, C. Liu, T. W. Noh, J. S. Lee, B. Kahng, J. H. Jang, M. Y. Kim, D.-W. Kim, C. U. Jung, *Appl. Phys. Lett.* **2008**, *92*, 183507.

[S7] We could not find the experimental result. We substituted the parameters of SiO_2 for Sm_2O_3.

[S8] Samarium(III) oxide, www.wikipedia.com, accessed: September, 2013.

[S9] We chose the parameters for the interface between those of Sm_2O_3 and $SrTiO_3$.

[S10] List of thermal conductivities, density and heat capacity of air, www.wikipedia.com, accessed: September, 2013.